Journal of Biomechanics ∎ (∎∎∎∎) ∎∎∎–∎∎∎

Contents lists available at ScienceDirect

Journal of Biomechanics

journal homepage: www.elsevier.com/locate/jbiomech
www.JBiomech.com

Simulations of morphotype-dependent hemodynamics in non-dilated bicuspid aortic valve aortas

Kai Cao [a], Samantha K. Atkins [a], Andrew McNally [a], Janet Liu [b], Philippe Sucosky [b,*]

[a] Department of Aerospace and Mechanical Engineering, University of Notre Dame, Notre Dame, IN, USA
[b] Department of Mechanical and Materials Engineering, Wright State University, Dayton, OH, USA

ARTICLE INFO

Article history:
Accepted 2 November 2016

Keywords:
Bicuspid aortic valve
Aorta
Hemodynamics
Hemodynamic stress
Aortic disease

ABSTRACT

Bicuspid aortic valves (BAVs) generate flow abnormalities that may promote aortopathy. While positive helix fraction (PHF) index, flow angle (θ), flow displacement (d) and wall shear stress (WSS) exhibit abnormalities in dilated BAV aortas, it is unclear whether those anomalies stem from the abnormal valve anatomy or the dilated aorta. Therefore, the objective of this study was to quantify the early impact of different BAV morphotypes on aorta hemodynamics prior to dilation. Fluid-structure interaction models were designed to quantify standard peak-systolic flow metrics and temporal WSS characteristics in a realistic non-dilated aorta connected to functional tricuspid aortic valve (TAV) and type-I BAVs. While BAVs generated increased helicity (PHF > 0.68) in the middle ascending aorta (AA), larger systolic flow skewness ($\theta > 11.2°$) and displacement ($d > 6.8$ mm) relative to the TAV (PHF=0.51; $\theta < 5.5°$; $d < 3.3$ mm), no distinct pattern was observed between morphotypes. In contrast, WSS magnitude and directionality abnormalities were BAV morphotype- and site-dependent. Type-I BAVs subjected the AA convexity to peak-systolic WSS overloads (up to 1014% difference vs. TAV). While all BAVs increased WSS unidirectionality on the proximal AA relative to the TAV, the most significant abnormality was achieved by the BAV with left-right-coronary cusp fusion on the wall convexity (up to 0.26 decrease in oscillatory shear index vs. TAV). The results indicate the existence of strong hemodynamic abnormalities in non-dilated type-I BAV AAs, their colocalization with sites vulnerable to dilation and the superior specificity of WSS metrics over global hemodynamic metrics to the valve anatomy.

© 2016 Elsevier Ltd. All rights reserved.

1. Introduction

The type-I bicuspid aortic valve (BAV) is the most common congenital cardiovascular defect and exists in different morphotypes, each with a distinct cusp fusion pattern (i.e., left-right-coronary cusp fusion (LR-BAV), right-non-coronary cusp fusion (RN-BAV) and non-left-coronary cusp fusion (NL-BAV)) (Ward, 2000). The BAV is a major risk factor for secondary aortopathy such as aortic dilation (Fedak et al., 2016; Michelena et al., 2011; Siu and Silversides, 2010), whose presentation depends on the BAV morphotype. While LR-BAVs are associated with aortic root dilation (type 1), RN- and NL-BAVs are more susceptible to dilation in the tubular portion of the ascending aorta (AA) (type 2) and in the proximal aortic arch (type 3) (Kang et al., 2013).

The dependence of the expression of aortopathy on the BAV subtype has suggested a role for hemodynamics in the etiology of BAV disease (Atkins and Sucosky, 2014). Flow eccentricity, skewness, helicity and wall shear stress (WSS) have been shown to be systematically higher in BAV aortas than in tricuspid aortic valve (TAV) aortas and to exhibit abnormalities in dilated BAV aorta regions (Barker et al., 2012; Bissell et al., 2013; Bonomi et al., 2015; Burris and Hope, 2015; Chandra et al., 2012; Mahadevia et al., 2014; Pasta et al., 2013; Seaman et al., 2014; van Ooij et al., 2015). While all these flow abnormalities may play different roles in BAV disease, they all impact the tissue via the interfacial fluid shear stress imposed on the endothelium. This observation combined with the established ability of vascular endothelial cells to sense and respond to changes in WSS magnitude, directionality and frequency through biological expression of cytokines, modulation of ion channels and smooth muscle cell signaling (Chiu and Chien, 2011; Lieu et al., 2004; Passerini et al., 2003) have suggested the key role played by WSS in BAV disease (Atkins et al., 2016a, 2016b). Despite the compelling evidence for the involvement of local flow abnormalities in the pathogenesis of BAV aortopathy, the existence of a

* Correspondence to: Department of Mechanical and Materials Engineering, Wright State University, 3640 Colonel Glenn Hwy, 257 Russ Engineering Center, Dayton, OH 45435, USA. Fax: +937 775 5082.
E-mail address: philippe.sucosky@wright.edu (P. Sucosky).

http://dx.doi.org/10.1016/j.jbiomech.2016.11.024
0021-9290/© 2016 Elsevier Ltd. All rights reserved.

hemodynamic etiology is still questionable as it is uncertain whether the reported flow abnormalities were due primarily to the valve morphology, the pre-existence of dilation in BAV patients, or anatomic differences between different patient cohorts. Addressing this uncertainty and isolating the early impact of the BAV anatomy on aortic flow require a controlled environment consisting of the same non-dilated aorta subjected to the flows of different BAV morphotypes. The present study aimed at addressing this need by examining computationally the early impact (i.e., prior to dilation) of different BAV morphotypes on the regional and temporal hemodynamic characteristics in a non-dilated aorta.

2. Materials and methods

2.1. Valve-aorta geometries

The three-dimensional valve-aorta geometry was designed in SolidWorks (Dassault Systemes, Inc) and consisted of the aortic root and the aorta (Fig. 1). The non-dilated aorta was reconstructed from a series of computed tomography images of a human aorta (Atkins et al., 2014; Cao and Sucosky, 2015) and consisted of the AA and the aortic arch along with brachiocephalic (BCA), left common carotid (LCCA) and left subclavian (LSCA) arteries. Consistent with our previous valve models (Cao et al., 2015; Cao and Sucosky, 2016), the TAV geometry consisted of three identical leaflets. Dimensional parameters for the aortic sinus and leaflets were obtained from published human aortic valve data (Thubrikar, 1989). The LR-BAV was constructed with a normal non-coronary leaflet and a larger leaflet mimicking fusion of the two coronary leaflets., The non-coronary leaflet and its sinus were designed to span a circumferential angle of 150° (Angelini et al., 1989; Sievers and Schmidtke, 2007). The left- and right-coronary leaflets were assumed to be identical and the raphe (i.e., line of fusion) was placed along the common free edge of these two leaflets. The RN-BAV and NL-BAV anatomies were obtained by rotating the entire LR-BAV valve apparatus (i.e., aortic root, aortic sinuses and leaflets) by 120° and 240°, respectively, about its axis.

2.2. FSI approach

The aortic wall and lumen were meshed with tetrahedral elements. In an effort to limit the computing time despite the large computational domain, the mesh strategy consisted of a coarser grid in the valvular flow region to generate qualitatively accurate flow patterns, and a finer grid with boundary layer treatment in the AA flow region where the WSS was to be analyzed. In addition, the structural domain was discretized using a coarser mesh than in the fluid domain since the focus of the study was on the flow characterization. Following a mesh sensitivity analysis, the final computational grid consisted of 70,000 elements in the structural domain (45,000 cells for the aorta and 25,000 cells for the aortic root and leaflets) and 1,014,000 elements in the fluid domain (632,000 cells in the aorta region and 382,000 cells in the valve region). This level of refinement achieved a spatial resolution of 80 μm near the aortic wall and generated only a 2% increase in peak-systolic WSS on the aortic wall relative to a mesh consisting of 25% smaller elements. Due to the implementation of an ALE FSI scheme, the mesh was automatically regenerated at time steps resulting in large structural deformations. The boundary layer mesh refinement was performed automatically on the fluid mesh generated at each time step. Fully coupled, two-way FSI simulations were performed in ANSYS 15.0 (ANSYS Inc.) using an arbitrary Lagrangian–Eulerian approach (Donea et al., 1982). The governing equations consisted of the momentum and continuity equations for the fluid domain, the momentum equation for the structure, and three coupling conditions enforcing continuity of displacements, velocities and tractions at the fluid-structure interface. The Navier–Stokes and continuity equations were solved using a finite volume method. The implicit flow solver used a second-order upwind spatial discretization scheme and a second-order temporal discretization scheme. The structural solver employed an implicit direct displacement-based finite element method. The system of equations was solved using the sparse direct solver and the equilibrium equations were solved by the Newton–Raphson method. A time step of 0.5 ms was implemented to discretize the entire cardiac cycle (0.86 s) and the simulations were run over three cardiac cycles to achieve temporal convergence.

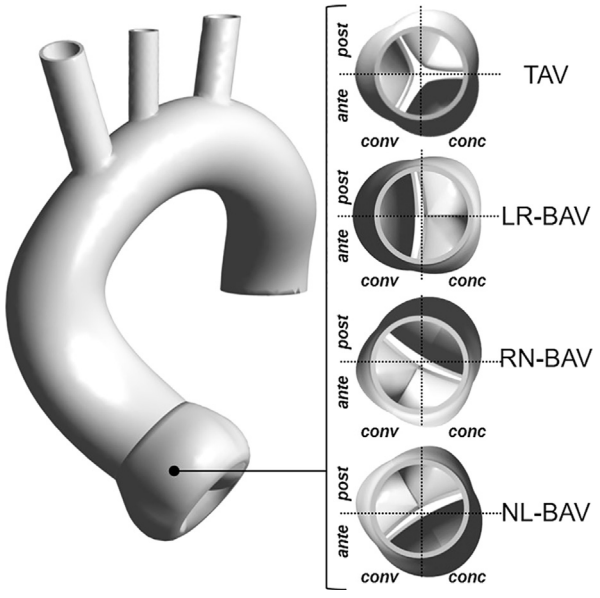


Fig. 1. Valve-aorta model and valve geometries (conv: convexity, conc: concavity, ante: anterior, post: posterior).

2.3. Material formulations and boundary conditions

The leaflet hyperelastic material was modeled using a previously published three-parameter incompressible Mooney–Rivlin model calibrated with respect to tensile test data on porcine leaflets (Cao et al., 2015). Consistent with previous artery and aorta models (Bathe and Kamm, 1999), the aortic wall was approximated as a linear, elastic, isotropic and nearly incompressible material (elastic modulus: 2 MPa; Poisson's ratio: 0.45). Blood was modeled as an incompressible, homogeneous and Newtonian fluid (density: 1050 kg/m^3; dynamic viscosity: 0.0035 Pa s). This approximation has been shown to generate less than 6% error in the predicted WSS on the leaflet fibrosa (i.e., low WSS region) relative to a non-Newtonian power-law model (Cao et al., 2015; Cao and Sucosky, 2016). The inlet boundary condition of the fluid domain consisted of a physiologic ventricular pressure waveform (0/120 mmHg, 2:1 diastolic/systolic ratio) and the four outlets of the aorta model (BCA, LCCA, LSCA and descending aorta) consisted of physiologic pressure waveforms obtained from the literature (Olufsen et al., 2000). The aortic wall was constrained in the axial direction at the inlet and outlet sections but was allowed to move in the radial and circumferential directions at all locations. A linear elastic support condition with a foundation stiffness of 75 mmHg/mm was prescribed on the outer aortic wall to simulate the damping effect generated by the surrounding tissues (Lantz et al., 2011). The implementation of the ALE strategy required a small 100-μm gap to be maintained between the leaflets in the coapted state. Frictionless conditions were prescribed between adjacent leaflets to simulate leaflet contact during coaptation. These conditions conditionally prevented leakage flow through the gap and treated the leaflets as in contact when the distance between two leaflets became smaller than 100 μm.

2.4. Flow characterization

Global aorta hemodynamics was assessed during the acceleration phase (t=70 ms), at peak systole (t=160 ms) and during the deceleration phase (t=240 ms) in terms of streamline, velocity and out-of-plane vorticity fields. All other flow characteristics were captured at common dilation sites for BAV aortas (Fig. 2A): 10 mm downstream of the sinotubular junction (proximal section, LR-BAV dilation) and 35 mm downstream of the sinotubular junction (middle section, NL-/RN-BAV dilation) (Agozzino et al., 2002; Evangelista et al., 2010). Flow helicity (Fig. 2B) was quantified in terms of the positive helix fraction (PHF) index (Faggiano et al., 2013),

$$\mathrm{PHF} = \frac{H_{pos}}{H_{pos} + H_{neg}}, \tag{1}$$

where H_{pos} and H_{neg} are the positive and negative parts, respectively, of the helicity flux over a section calculated as:

$$H = \int_S (\nabla \times ((\mathbf{V} \cdot \hat{\mathbf{t}})\hat{\mathbf{t}})) \cdot \hat{\mathbf{n}}\, dS \tag{2}$$

($\mathbf{V}$: velocity vector, $\hat{\mathbf{t}}$: unit vector tangent to the section, $\hat{\mathbf{n}}$: unit vector normal to the section, dS: surface element). The PHF represents the ratio of right-handed flows to the total helical flows over a section (PHF=0: purely left-handed helical flow; PHF=1: purely right-handed helical flow). Valvular jet skewness and eccentricity were quantified in terms of the flow angle θ (i.e., angle between the mean flow vector and the unit vector normal to the section of interest (Mahadevia et al., 2014); Fig. 2C), and flow displacement d (i.e., distance between the center of the section of interest and the centroid of the top 15% of velocities in the same section (Sigovan et al., 2011); Fig. 2D), respectively. The longitudinal (i.e., streamwise) WSS τ was captured at 20 points along the wall circumference in the proximal and middle AA

Please cite this article as: Cao, K., et al., Simulations of morphotype-dependent hemodynamics in non-dilated bicuspid aortic valve aortas. Journal of Biomechanics (2016), http://dx.doi.org/10.1016/j.jbiomech.2016.11.024

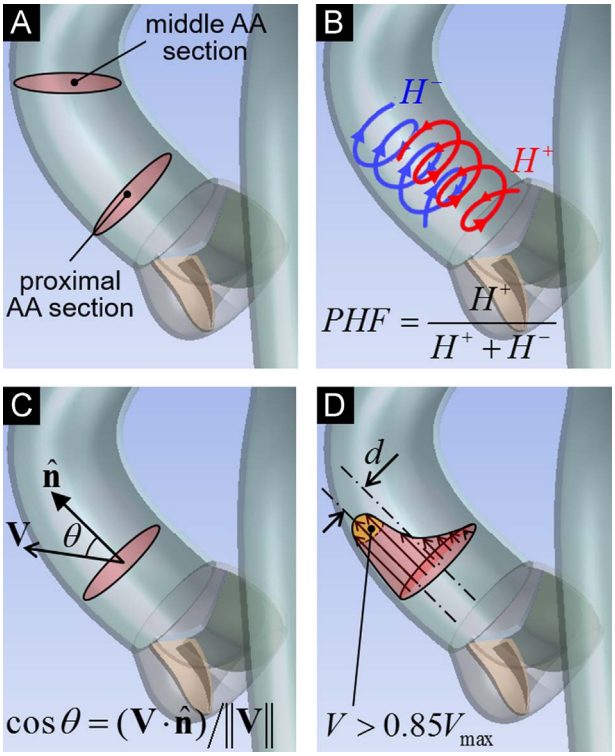


Fig. 2. Hemodynamic characterization: A) investigation sites; B) PHF definition; C) flow angle definition; and D) flow displacement definition.

sections and its temporal characteristics were further assessed in terms of peak-systolic magnitude (pWSS), temporal shear magnitude (TSM),

$$\mathrm{TSM} = \frac{1}{T}\int_0^T |\tau| dt, \tag{3}$$

and oscillatory shear index (OSI),

$$\mathrm{OSI} = \frac{1}{2}\left[1 - \left(\left|\int_0^T \tau dt\right| \Big/ \int_0^T |\tau| dt\right)\right]. \tag{4}$$

The TSM is a measure of the time-averaged WSS magnitude over one cardiac cycle, while the OSI characterizes the oscillatory nature of the WSS signal (OSI=0: purely unidirectional; OSI=0.5: purely oscillatory).

3. Results

3.1. General flow characteristics

Under the same transvalvular pressure, the BAVs generated a lower cardiac output (4.0 L/min) than the TAV (4.5 L/min), suggesting an intrinsic degree of stenosis in type-I BAVs. These results are within the range reported by clinical studies for BAV patients (average cardiac output: 3.5 ± 1.3 L/min (Barker et al., 2010; Mirabella et al., 2015)). The TAV generates a streamline field essentially parallel to the aortic wall, with only a few helical peripheral streamlines due to the flow development along the curved wall (Fig. 3A). While the BAVs exhibit similar characteristics during the acceleration phase, the helicity of their peripheral streamlines is more intense and widespread from peak systole throughout the deceleration phase. Analysis of the maximum flow velocities (Fig. 3B) reveals the weak impact of the BAV morphotype (less than 4% difference in maximum velocity between all BAV throughout the cardiac cycle) and confirms the stenotic nature of type-I BAVs (up to 39% increase in maximum velocity vs. TAV at peak systole). Animations of the streamline and velocity fields predicted in all models are provided as online Supplementary material (Videos 1 and 2, respectively).

Supplementary material related to this article can be found online at http://dx.doi.org/10.1016/j.jbiomech.2016.11.024.

3.2. Peak-systolic flow vorticity and helicity

At peak systole, while the BAVs generate more intense vorticity (>55.9/s) than the TAV (32.2/s) in the proximal AA (Fig. 4A), TAV and BAV flows captured in that section are characterized by the coexistence of right- and left-handed helical flow patterns of equal intensity with no prevailing direction ($0.50 < \mathrm{PHF} < 0.52$, Fig. 4B). The progressive development of the flow along the aorta results in a dramatic increase in vorticity in the middle AA of all BAV models (section-averaged vorticity >102.9/s) with intense right-handed helicity in the anterior region ($0.68 < \mathrm{PHF} < 0.72$). These characteristics contrast with those captured in the same section downstream of the TAV (mean vorticity=61.0/s; PHF=0.51). The PHF is weakly dependent on the BAV morphotype (less than 4% and 6% difference in PHF between BAV morphotypes in the proximal and middle AA, respectively).

3.3. Flow skewness and eccentricity

In the proximal AA, the TAV and BAVs generate a central peak-systolic orifice jet whose section mimics the respective geometry of the valve opening (i.e., three-lobed shape for the TAV and elliptical shape for the BAVs, Fig. 5A). In the middle AA, the development of the flow along the wall curvature is accompanied by the progressive migration of the high-momentum jet toward the posterior region of the aortic wall. The jet characteristics captured in the proximal section reveal higher degrees of skewness and eccentricity for the BAVs ($\theta > 11.2°$, $d > 4.9$ mm) relative to the TAV ($\theta = 4.6°$, $d = 1.3$ mm) (Fig. 5B and C). Although the same trend is observed in the middle section, the degree of discrepancy is slightly attenuated (BAV jet: $\theta > 12.1°$, $d > 6.8$ mm; TAV jet: $\theta = 5.5°$, $d = 3.3$ mm). The BAV flow characteristics exhibit a strong dependence on the valve morphotype. While the NL-BAV generates the most pronounced abnormality in jet angle in the proximal and middle AA ($\theta = 13.8°$ and $13.6°$, respectively) relative to the two other morphotypes ($\theta < 12.4°$ and $\theta < 13.4°$, respectively), the most substantial anomalies in flow displacement are achieved by the LR-BAV in the proximal AA ($d = 6.9$ mm vs. $d < 5.1$ mm for other morphotypes) and by the RN-BAV in the middle AA ($d = 8.5$ mm vs. $d < 8.0$ mm for other morphotypes).

3.4. Regional WSS characteristics

Animations of the WSS fields predicted in all models are provided as online Supplementary material (Video 3).

Supplementary material related to this article can be found online at http://dx.doi.org/10.1016/j.jbiomech.2016.11.024.

3.4.1. Peak-systolic WSS magnitude (pWSS)

In the proximal AA, the particular symmetry and central alignment of the TAV jet result in a moderate and positive pWSS environment (section-averaged pWSS $= +35.2$ dyn/cm^2) (Fig. 6A). In contrast, the helicity of the peripheral BAV streamlines subjects the proximal AA to a negative pWSS oriented against the jet direction (section-averaged pWSS < -18.3 dyn/cm^2). In addition, while the valve anatomy only has a slight impact on pWSS magnitude on the wall concavity (between 7% and 23% difference between TAV and BAVs), it affects it more substantially on the wall

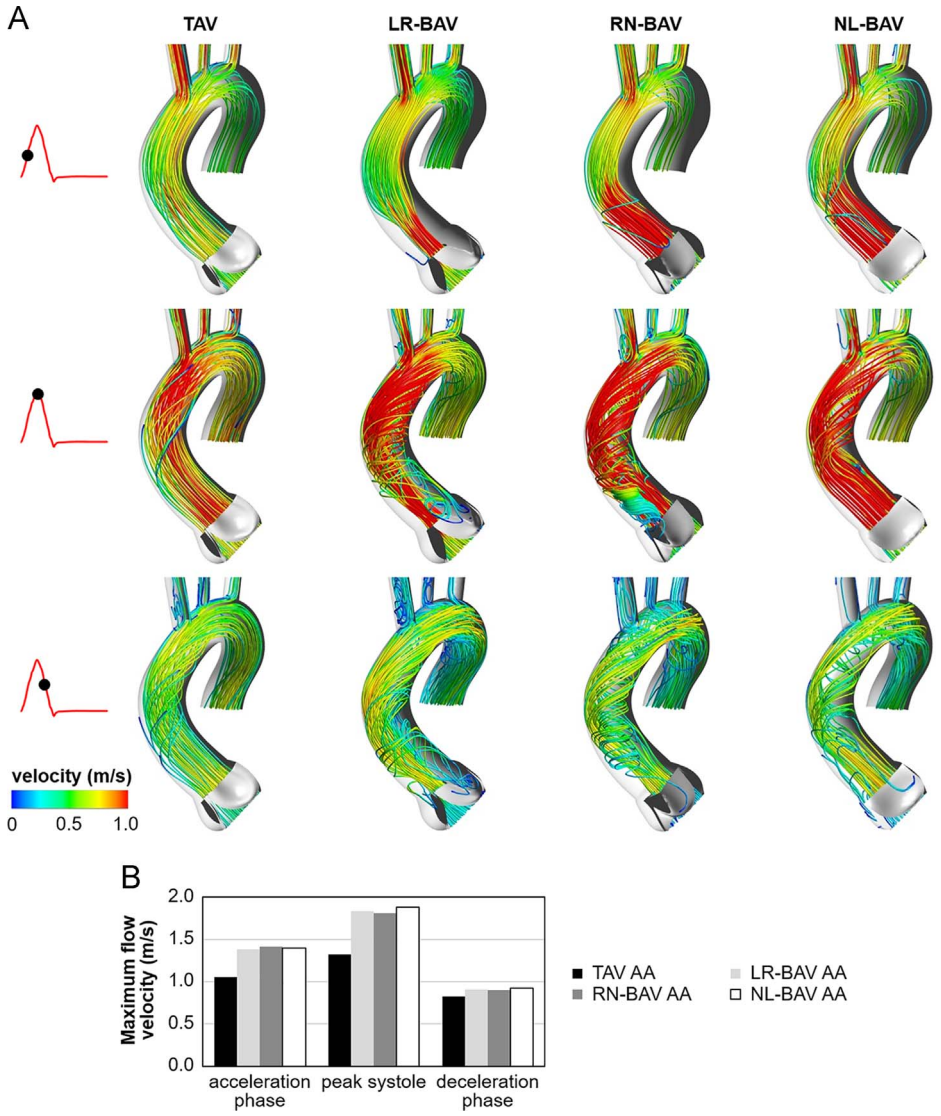


Fig. 3. Flow streamlines and velocities: A) streamline field; and B) maximum flow velocities predictions during the acceleration phase, at peak systole and during the deceleration phase.

convexity (between 12% and 168% difference between TAV and BAVs) (Fig. 6B). In the middle AA, the progressive development of the flow along the aorta normalizes pWSS directionality in the streamwise direction ($pWSS > 0$) in all models. Repeating the trend observed in the proximal section, BAVs subject the wall concavity to essentially similar pWSS underloads relative to the TAV (between 49% and 58% reduction vs. TAV), while generating morphotype-dependent pWSS levels on the wall convexity (8% to 62% difference vs. TAV).

3.4.2. Temporal Shear Magnitude (TSM)

In the proximal AA, the TAV generates an essentially uniform (Fig. 6A) and moderate TSM distribution (18% difference between convexity and concavity, Fig. 6C). The LR-BAV subjects the proximal AA to WSS overloads (convexity: 26% increase; concavity: 32% increase in TSM vs. TAV). In contrast, the RN-BAV and NL-BAV generate side-specific WSS magnitude abnormalities (up to 57% overload in the convexity; up to 13% underload in the concavity). The downstream normalization of BAV flow results in side-specific TSM distributions in the middle AA characterized by morphotype-dependent overloads on the wall convexity (between 14% and 70% increase vs. TAV) and relatively similar underloads on the concavity (between 25% and 34% decrease vs. TAV).

3.4.3. Oscillatory Shear Index (OSI)

In the proximal AA, the TAV generates essentially bidirectional and oscillatory WSS (convexity OSI=0.36; concavity OSI=0.38) (Fig. 6A and D). In contrast, all BAVs subject the wall to a more pulsatile and unidirectional WSS environment (convexity $OSI < 0.24$; concavity $OSI < 0.20$), with the LR-BAV and NL-BAV generating the highest degree of WSS directionality abnormality on the convexity (0.26 reduction in OSI vs. TAV) and concavity (0.27 reduction in OSI vs. TAV), respectively. In the middle AA, WSS directionality is more consistent among the four valves and exhibits a high degree of unidirectionality on the wall convexity ($OSI < 0.10$) and more bidirectionality on the wall concavity ($OSI > 0.23$). In this section, the highest degree of WSS directionality abnormality is generated by the RN-BAV and NL-BAV on the wall convexity (up to 0.07 reduction in OSI vs. TAV) and by the LR-BAV on the wall concavity (0.15 increase in OSI vs. TAV).

Please cite this article as: Cao, K., et al., Simulations of morphotype-dependent hemodynamics in non-dilated bicuspid aortic valve aortas. Journal of Biomechanics (2016), http://dx.doi.org/10.1016/j.jbiomech.2016.11.024

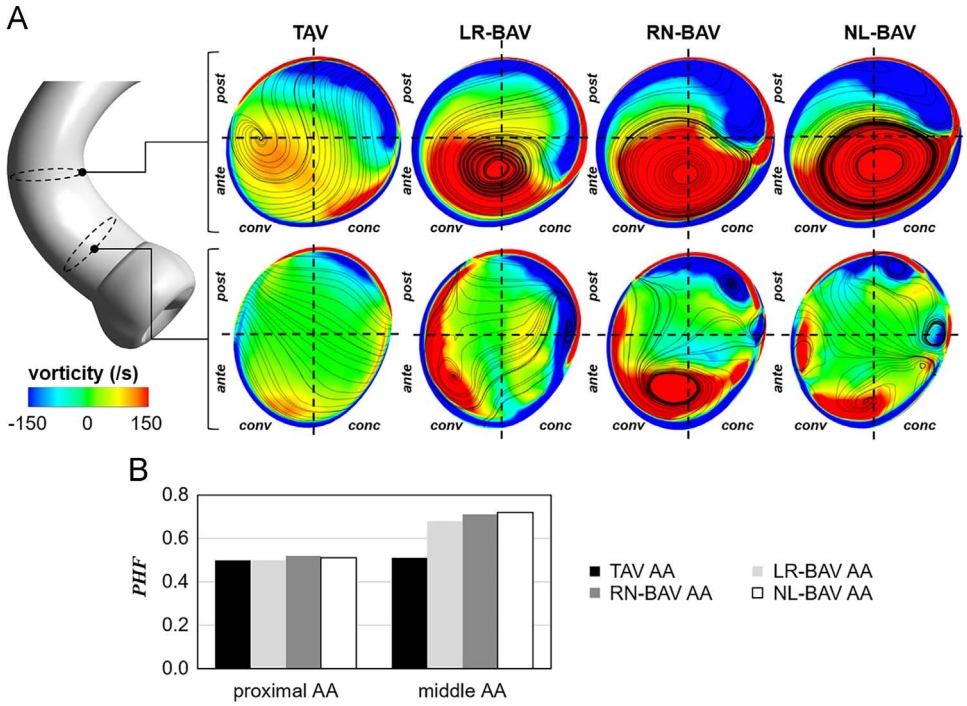


Fig. 4. Peak-systolic flow vorticity and helicity: A) out-of-plane vorticity fields captured in the proximal and middle AA sections (conv: convexity, conc: concavity, ante: anterior, post: posterior); and B) positive helix fraction predictions during the acceleration phase, at peak systole and during the deceleration phase.

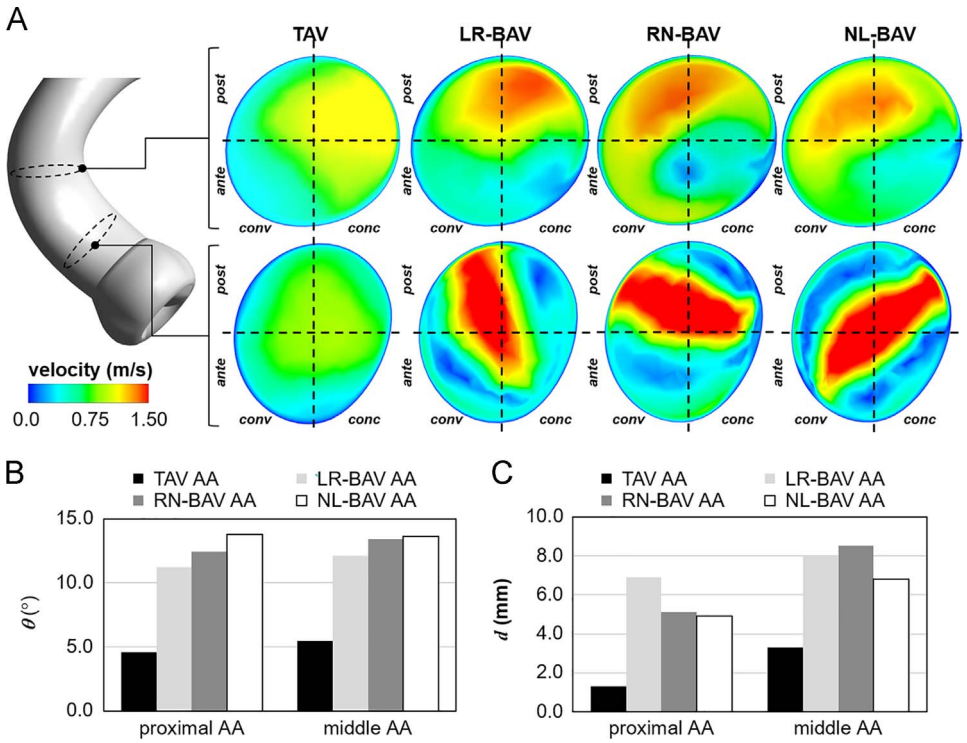


Fig. 5. Peak-systolic flow velocity, skewness and eccentricity: A) velocity fields captured in the proximal and middle AA sections (conv: convexity, conc: concavity, ante: anterior, post: posterior); B) flow angle predictions; and C) flow displacement predictions during the acceleration phase, at peak systole and during the deceleration phase.

4. Discussion

4.1. BAV AA hemodynamic abnormalities

The present study demonstrates that the main four hemodynamic hallmarks of BAV flow are eccentricity, skewness, stenosis and right-handed helicity. Although those findings are consistent with previous MRI reports (Barker et al., 2010; Bissell et al., 2013; Mahadevia et al., 2014), the demonstration of their validity in a normal aorta provides strong evidence for their universality among all type-I BAV aortas, regardless of their degree of dilation.

Please cite this article as: Cao, K., et al., Simulations of morphotype-dependent hemodynamics in non-dilated bicuspid aortic valve aortas. Journal of Biomechanics (2016), http://dx.doi.org/10.1016/j.jbiomech.2016.11.024

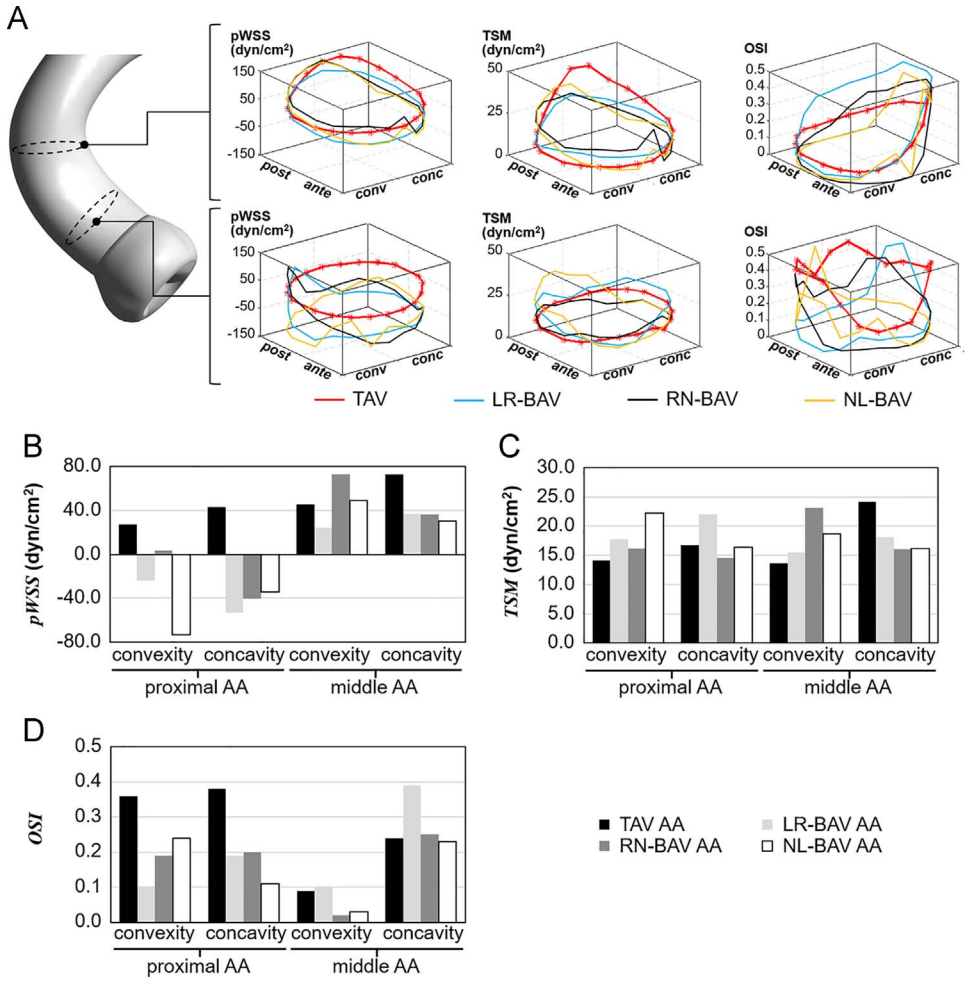


Fig. 6. Regional WSS characteristics: A) pWSS, TSM and OSI distributions along the AA circumference; and B) side-specific predictions in the proximal and middle AA sections.

4.2. *Effects of leaflet fusion type on global flow metrics and WSS characteristics*

Global flow characteristics such as eccentricity, skewness, peak velocity and helicity did not exhibit strong specificity to the BAV morphotype in a non-dilated aorta. While peak-systolic flow velocity indicated the existence of a stenotic jet in all BAV AAs, it was weakly affected by the type of cusp fusion. The PHF not only failed at exhibiting any specificity to the BAV morphotype, it was also unable to differentiate TAV and BAV flows in the proximal AA. Lastly, flow angle and displacement were sensitive to the abnormal bicuspid anatomy but were slightly impacted by the leaflet fusion pattern. In contrast, WSS characteristics exhibited more specificity to the BAV morphotype and this specificity was site-dependent. pWSS was strongly affected by the leaflet fusion type on the AA convexity but less on the concavity. Similarly, while all BAVs generated an abnormal unidirectional WSS environment on the proximal AA wall, the circumferential OSI distribution exhibited a strong dependence on the leaflet fusion. Opposing this trend, the analysis of the TSM revealed the weak dependence of this metric on the BAV morphotype and its limited streamwise and circumferential variability along the AA wall.

4.3. *Effects of aortic dilation on BAV hemodynamics*

The comparison of the present results in a non-dilated aorta to previous clinical measurements in dilated BAV aortas provides critical insights into the respective contribution of the valve anatomy and aorta anatomy on aortic flow. The flow angles predicted in non-dilated LR-BAV and RN-BAV aortas are not only systematically lower (up to 54% reduction) than those measured previously in dilated aortas (Bissell et al., 2013; Mahadevia et al., 2014), they are also less specific to the BAV morphotype (non-dilated aorta: 11% difference between the two morphotypes in the middle AA; dilated aorta: 52% difference). Similar discrepancies are obtained with flow displacement, whose values in the proximal and middle section of non-dilated AAs are up to 24% lower and 40% larger, respectively, than those measured in vivo in dilated aortas (Mahadevia et al., 2014). Lastly, the degree of AA enlargement impacts both the specificity of pWSS to the BAV morphotype, which is high in non-dilated LR-BAV and RN-BAV AAs but low in dilated AAs, but also the sign of this quantity, which is negative in the proximal region in non-dilated AAs but systematically positive in dilated BAV AAs (Bissell et al., 2013; Hope et al., 2011; Mahadevia et al., 2014). Overall, those results suggest that global flow metrics may be more affected by the enlargement of the aorta than by the valve anatomy.

4.4. *Clinical implications*

The characterization of the early impact of the BAV on aortic flow prior to dilation fills a knowledge gap that may be critical to the elucidation of BAV aortopathy.

While flow angle has been proposed as a robust predictor of aortic dilation in BAV patients due to its strong specificity to the BAV morphotype and its significant abnormality relative to TAV aortas (Mahadevia et al., 2014; Sigovan et al., 2011), the present

Please cite this article as: Cao, K., et al., Simulations of morphotype-dependent hemodynamics in non-dilated bicuspid aortic valve aortas. Journal of Biomechanics (2016), http://dx.doi.org/10.1016/j.jbiomech.2016.11.024

results indicate only slight differences in flow angle between the three non-dilated type-I BAV AAs. This suggests that the observed variability in flow angle between different BAV morphotypes might be an artifact of an enlarged aorta rather than a robust marker of morphotype-dependent hemodynamics.

In contrast, WSS directionality (as quantified by OSI) was identified in this study as the characteristic most affected by the presence of a BAV and most specific to the BAV morphotype. Abnormally low OSI levels were isolated in the convexity of the proximal LR-BAV AA and the middle RN-BAV and NL-BAV AAs (i.e., regions prone to dilation), suggesting a correlation between WSS directionality abnormalities and aortopathy expression. Importantly, in the LR-BAV AA, the contrasted WSS directionalities on the convexity and concavity of the proximal wall were associated with similar TSM environments (high on both sides), which rules out WSS magnitude abnormalities as a decisive driver for aortopathy. The sensitivity of aortic tissue to OSI abnormalities has been verified ex vivo. Studies conducted in our laboratory have demonstrated a significant upregulation of matrix metalloproteinase expression and activity in aortic tissue subjected to WSS isolated from the proximal convexity of the LR-BAV AA but no change in response to WSS isolated from the concavity relative to tissue subjected to TAV WSS (Atkins et al., 2014, 2016b). This response correlates with the asymmetric presentation of aortic dilation in LR-BAV patients (Cotrufo et al., 2005) and could also explain the apparent parallel between the unidirectional WSS environments generated by the RN-BAV and NL-BAV in the middle AA and the particular vulnerability of this region to dilation (Bissell et al., 2013; Kang et al., 2013; Mahadevia et al., 2014).

While those observations suggest the key role and the potential prognostic value of OSI in BAV aortopathy, the measurement of this metric in vivo is challenging due to the need for high temporal and spatial resolutions near the aortic wall. The development of improved flow assessment techniques harnessing the convenience of standard imaging modalities and the high resolutions provided by computational fluid dynamics modeling may enable the use of OSI as a clinical prognostic tool for BAV aortopathy.

5. Limitations

The models could benefit from several improvements. The anisotropy of the leaflet material was discarded in these simulations. While our previous FSI study of the aortic valve has demonstrated the limited effects of this simplifying assumption on valvular hemodynamics (Cao and Sucosky, 2016), the inclusion of tissue anisotropy would improve leaflet dynamics. In addition, the simulations did not account for the effects of turbulence. While those could be simulated via implementation of direct numerical simulations, this strategy is computationally expensive and impractical in a context of FSI simulations. Lastly, the study only focused on flow-related characteristics and did not investigate any structural stress abnormality. This choice was motivated by the demonstrated ability of isolated BAV WSS abnormalities to trigger a remodeling response in aortic tissue (Atkins et al., 2014, 2016b). It is expected that structural abnormalities in the aortic wall may become increasingly significant as dilation develops and may contribute to disease progression at a later stage.

6. Conclusions

In summary, this study reveals: 1) the existence of strong hemodynamic abnormalities in non-dilated type-I BAV AAs, 2) the superior specificity of regional WSS metrics over global hemodynamic metrics to the BAV morphotype, and 3) the colocalization of WSS directionality abnormalities and sites prone to dilation in non-dilated type-I BAV AAs. Those results suggest that global flow metrics currently considered in the clinic for the assessment of BAV hemodynamics (e.g., flow skewness, eccentricity, velocity) may not be sufficient to grasp the complexity of BAV flow and the mechanical abnormalities that it generates on the aortic wall. The improvement of in vivo imaging techniques toward the precise assessment of near-wall hemodynamics and temporal WSS metrics in BAV aortas may enable the development of new clinical tools for the detection and prognosis of BAV aortopathy.

Conflict of interest statement

None declared.

Acknowledgments

This work was in part supported by National Science Foundation (NSF) Grants CMMI-1148558 and CMMI-1550144 and American Heart Association (AHA) Grant 14PRE18940010.

References

Agozzino, L., Ferraraccio, F., Esposito, S., Trocciola, A., Parente, A., Della Corte, A., De Feo, M., Cotrufo, M., 2002. Medial degeneration does not involve uniformly the whole ascending aorta: morphological, biochemical and clinical correlations. Eur. J. Cardiothorac. Surg. 21, 675–682. http://dx.doi.org/10.1016/S1010-7940(02)00022-2.

Angelini, A., Ho, S.Y., Anderson, R.H., Devine, W.A., Zuberbuhler, J.R., Becker, A.E., Davies, M.J., 1989. The morphology of the normal aortic valve as compared with the aortic valve having two leaflets. J. Thorac. Cardiovasc. Surg. 98, 362–367.

Atkins, S.K., Sucosky, P., 2014. The etiology of bicuspid aortic valve disease: focus on hemodynamics. World J. Cardiol. 12, 1227–1233. http://dx.doi.org/10.4330/wjc.v6.i12.1227.

Atkins, S.K., McNally, A., Sucosky, P., 2016a. Mechanobiology in cardiovascular disease management: potential strategies and current needs. Front. Bioeng. Biotechnol. 4, 79. http://dx.doi.org/10.3389/fbioe.2016.00079.

Atkins, S.K., Moore, A., Sucosky, P., 2016b. Bicuspid aortic valve hemodynamics does not promote remodeling in porcine aortic wall concavity. World J. Cardiol. 8, 89–97. http://dx.doi.org/10.4330/wjc.v8.i1.89.

Atkins, S.K., Cao, K., Rajamannan, N.M., Sucosky, P., 2014. Bicuspid aortic valve hemodynamics induces abnormal medial remodeling in the convexity of porcine ascending aortas. Biomech. Model. Mechanobiol. 13, 1209–1225. http://dx.doi.org/10.1007/s10237-014-0567-7.

Barker, A.J., Lanning, C., Shandas, R., 2010. Quantification of hemodynamic wall shear stress in patients with bicuspid aortic valve using phase-contrast MRI. Ann. Biomed. Eng. 38, 788–800. http://dx.doi.org/10.1007/s10439-009-9854-3.

Barker, A.J., Markl, M., Bürk, J., Lorenz, R., Bock, J., Bauer, S., Schulz-Menger, J., von Knobelsdorff-Brenkenhoff, F., 2012. Bicuspid aortic valve is associated with altered wall shear stress in the ascending aorta. Circ. Cardiovasc. Imaging 5, 457–466. http://dx.doi.org/10.1161/CIRCIMAGING.112.973370.

Bathe, M., Kamm, R.D., 1999. A fluid-structure interaction finite element analysis of pulsatile blood flow through a compliant stenotic artery. J. Biomech. Eng. 121, 361–369. http://dx.doi.org/10.1115/1.2798332.

Bissell, M.M., Hess, A.T., Biasiolli, L., Glaze, S.J., Loudon, M., Pitcher, A., Davis, A., Prendergast, B., Markl, M., Barker, A.J., Neubauer, S., Myerson, S.G., 2013. Aortic dilation in bicuspid sortic valve disease: flow pattern is a major contributor and differs with valve. Fusion Type Circ. Cardiovasc. Imaging 6, 499–507. http://dx.doi.org/10.1161/CIRCIMAGING.113.000528.

Bonomi, D., Vergara, C., Faggiano, E., Stevanella, M., Conti, C., Redaelli, A., Puppini, G., Faggian, G., Formaggia, L., Luciani, G.B., 2015. Influence of the aortic valve leaflets on the fluid-dynamics in aorta in presence of a normally functioning bicuspid valve. Biomech. Model. Mechanobiol. . http://dx.doi.org/10.1007/s10237-015-0679-8

Burris, N.S., Hope, M.D., 2015. Bicuspid valve-related aortic disease: flow assessment with conventional phase-contrast MRI. Acad. Radiol. 22 (6), 690. http://dx.doi.org/10.1016/j.acra.2015.01.010.

Cao, K., Sucosky, P., 2015. Effect of bicuspid aortic valve cusp fusion on aorta wall shear stress: preliminary computational assessment and implication for aortic dilation. World J. Cardiovasc. Dis. 5, 129–140. http://dx.doi.org/10.4236/wjcd.2015.56016.

Cao, K., Sucosky, P., 2016. Computational comparison of regional stress and deformation characteristics in tricuspid and bicuspid aortic valve leaflets. Int. J. Numer. Methods Biomed. Eng. . http://dx.doi.org/10.1002/cnm.2798

Cao, K., Bukač, M., Sucosky, P., 2015. Three-dimensional macro-scale assessment of regional and temporal wall shear stress characteristics on aortic valve leaflets.

Comput. Methods Biomech. Biomed. Eng., 1–11. http://dx.doi.org/10.1080/10255842.2015.1052419.

Chandra, S., Rajamannan, N.M., Sucosky, P., 2012. Computational assessment of bicuspid aortic valve wall-shear stress: implications for calcific aortic valve disease. Biomech. Model. Mechanobiol. 11, 1085–1096. http://dx.doi.org/10.1007/s10237-012-0375-x.

Chiu, J.-J., Chien, S., 2011. Effects of disturbed flow on vascular endothelium: pathophysiological basis and clinical perspectives. Physiol. Rev. 91, 327–387. http://dx.doi.org/10.1152/physrev.00047.2009.

Cotrufo, M., Della Corte, A., De Santo, L.S., Quarto, C., De Feo, M., Romano, G., Amarelli, C., Scardone, M., Di Meglio, F., Guerra, G., Scarano, M., Vitale, S., Castaldo, C., Montagnani, S., 2005. Different patterns of extracellular matrix protein expression in the convexity and the concavity of the dilated aorta with bicuspid aortic valve: preliminary results. J. Thorac. Cardiovasc. Surg. 130, 504–511. http://dx.doi.org/10.1016/j.jtcvs.2005.01.016.

Donea, J., Guiliani, S., Halleux, J.P., 1982. An abitrary Lagrangian–Eulerian finite-element method for transient dynamic fluid structure interactions. Comput. Methods Appl. Mech. Eng. 33, 689–723. http://dx.doi.org/10.1016/0045-7825(82)90128-1.

Evangelista, A., Flachskampf, F.A., Erbel, R., Antonini-Canterin, F., Vlachopoulos, C., Rocchi, G., Sicari, R., Nihoyannopoulos, P., Zamorano, J., Pepi, M., Breithardt, O.-A., Plonska-Gosciniak, E., 2010. Echocardiography in aortic diseases: eae recommendations for clinical practice. Eur. J. Echocardiogr. 11, 645–658. http://dx.doi.org/10.1093/ejechocard/jeq056.

Faggiano, E., Antiga, L., Puppini, G., Quarteroni, A., Luciani, G.B., Vergara, C., 2013. Helical flows and asymmetry of blood jet in dilated ascending aorta with normally functioning bicuspid valve. Biomech. Model. Mechanobiol. 12, 801–813. http://dx.doi.org/10.1007/s10237-012-0444-1.

Fedak, P.W.M., Barker, A.J., Verma, S., 2016. Year in review: bicuspid aortopathy. Curr. Opin. Cardiol. 31, 132–138. http://dx.doi.org/10.1097/HCO.0000000000000258.

Hope, M.D., Hope, T.A., Crook, S.E.S., Ordovas, K.G., Urbania, T.H., Alley, M.T., Higgins, C.B., 2011. 4D flow CMR in assessment of valve-related ascending aortic disease. JACC Cardiovasc. Imaging 4 (7), 781. http://dx.doi.org/10.1016/j.jcmg.2011.05.004.

Kang, J.-W., Song, H.G., Yang, D.H., Baek, S., Kim, D.-H., Song, J.-M., Kang, D.-H., Lim, T.-H., Song, J.-K., 2013. Association between bicuspid aortic valve phenotype and patterns of valvular dysfunction and bicuspid aortopathy: comprehensive evaluation using MDCT and echocardiography. JACC Cardiovasc. Imaging 6, 150–161. http://dx.doi.org/10.1016/j.jcmg.2012.11.007.

Lantz, J., Renner, J., Karlsson, M., 2011. Wall shear stress in a subject specific human aorta – influence of fluid-structure interaction. Int. J. Appl. Mech. 3, 759–778. http://dx.doi.org/10.1142/S1758825111001226.

Lieu, D.K., Pappone, P.A., Barakat, A.I., 2004. Differential membrane potential and ion current responses to different types of shear stress in vascular endothelial cells. Am. J. Physiol. Cell Physiol. 286, C1367–C1375. http://dx.doi.org/10.1152/ajpcell.00243.2003.

Mahadevia, R., Barker, A.J., Schnell, S., Entezari, P., Kansal, P., Fedak, P.W.M., Malaisrie, S.C., McCarthy, P., Collins, J., Carr, J., Markl, M., 2014. Bicuspid aortic cusp fusion morphology alters aortic 3D outflow patterns, wall shear stress and expression of aortopathy. Circulation 129, 673–682. http://dx.doi.org/10.1161/CIRCULATIONAHA.113.003026.

Michelena, H.I., Khanna, A.D., Mahoney, D., Margaryan, E., Topilsky, Y., Suri, R.M., Eidem, B., Edwards, W.D., Sundt, T.M., Enriquez-Sarano, M., 2011. Incidence of aortic complications in patients with bicuspid aortic valves. JAMA 306, 1104–1112. http://dx.doi.org/10.1001/jama.2011.1286.

Mirabella, L., Barker, A.J., Saikrishnan, N., Coco, E.R., Mangiameli, D.J., Markl, M., Yoganathan, A.P., 2015. MRI-based protocol to characterize the relationship between bicuspid aortic valve morphology and hemodynamics. Ann. Biomed. Eng 43, 1815–1827. http://dx.doi.org/10.1007/s10439-014-1214-2.

Olufsen, M.S., Peskin, C.S., Kim, W.Y., Pedersen, E.M., Nadim, A., Larsen, J., 2000. Numerical simulation and experimental validation of blood flow in arteries with structured-tree outflow conditions. Ann. Biomed. Eng. 28, 1281–1299. http://dx.doi.org/10.1114/1.1326031.

Passerini, A.G., Milsted, A., Rittgers, S.E., 2003. Shear stress magnitude and directionality modulate growth factor gene expression in preconditioned vascular endothelial cells. J. Vasc. Surg. 37, 182–190. http://dx.doi.org/10.1067/mva.2003.66.

Pasta, S., Rinaudo, A., Luca, A., Pilato, M., Scardulla, C., Gleason, T.G., Vorp, D.A., 2013. Difference in hemodynamic and wall stress of ascending thoracic aortic aneurysms with bicuspid and tricuspid aortic valve. J. Biomech. 46, 1729–1738. http://dx.doi.org/10.1016/j.jbiomech.2013.03.029.

Seaman, C., Akingba, A., Sucosky, P., 2014. Steady flow hemodynamic and energy loss measurements in normal and simulated calcified tricuspid and bicuspid aortic valves. J. Biomech. Eng. 136, 1–11. http://dx.doi.org/10.1115/1.4026575.

Sievers, H., Schmidtke, C., 2007. A classification system for the bicuspid aortic valve from 304 surgical specimens. J. Thorac. Cardiovasc. Surg. 133, 1226–1233. http://dx.doi.org/10.1016/j.jtcvs.2007.01.039.

Sigovan, M., Hope, M.D., Dyverfeldt, P., Saloner, D., 2011. Comparison of four-dimensional flow parameters for quantification of flow eccentricity in the ascending aorta. J. Magn. Reson. Imaging 34, 1226–1230. http://dx.doi.org/10.1002/jmri.22800.

Siu, S.C., Silversides, C.K., 2010. Bicuspid aortic valve disease. J. Am. Coll. Cardiol. 55, 2789–2800. http://dx.doi.org/10.1016/j.jacc.2009.12.068.

Thubrikar, M.J., 1989. The Aortic Valve. CRC Press Inc., Boca Raton, FL.

van Ooij, P., Potters, W.V., Collins, J., Carr, M., Carr, J., Malaisrie, S.C., Fedak, P.W.M., McCarthy, P.M., Markl, M., Barker, A.J., 2015. Characterization of abnormal wall shear stress using 4D flow MRI in human bicuspid aortopathy. Ann. Biomed. Eng. 43, 1385–1397. http://dx.doi.org/10.1007/s10439-014-1092-7.

Ward, C., 2000. Clinical significance of the bicuspid aortic valve. Heart 83, 81–85. http://dx.doi.org/10.1136/heart.83.1.81.

Please cite this article as: Cao, K., et al., Simulations of morphotype-dependent hemodynamics in non-dilated bicuspid aortic valve aortas. Journal of Biomechanics (2016), http://dx.doi.org/10.1016/j.jbiomech.2016.11.024